

COMBINING COMPRESSED SENSING WITH MOTION CORRECTION IN ACQUISITION AND RECONSTRUCTION FOR PET/MR

Thomas Küstner^{*†} Christian Würslin[†] Holger Schmidt[†] Bin Yang^{*}

^{*} Institute of Signal Processing and System Theory, University of Stuttgart, Stuttgart, Germany

[†] Department of Radiology, University of Tübingen, Tübingen, Germany

ABSTRACT

In the field of oncology, simultaneous Positron-Emission-Tomography/Magnetic Resonance (PET/MR) scanners offer a great potential for improving diagnostic accuracy. However, to achieve a high Signal-to-Noise Ratio (SNR) for an accurate lesion detection and quantification in the PET/MR images, one has to overcome the induced respiratory motion artifacts. The simultaneous acquisition allows performing a MR-based non-rigid motion correction of the PET data. It is essential to acquire a 4D (3D + time) motion model as accurate and fast as possible to minimize additional MR scan time overhead. Therefore, a Compressed Sensing (CS) acquisition by means of a variable-density Gaussian subsampling is employed to achieve high accelerations. Reformulating the sparse reconstruction as a combination of the inverse CS problem with a non-rigid motion correction improves the accuracy by alternately projecting the reconstruction results on either the motion-compensated CS reconstruction or on the motion model optimization. *In-vivo* patient data substantiates the diagnostic improvement.

Index Terms— Compressed Sensing, sparse representation, Motion Correction, Medical Image Processing, PET/MR

1. INTRODUCTION

The hybrid Positron-Emission Tomography/Magnetic Resonance (PET/MR) technology offers the possibility to combine the high resolution of MR imaging with the high molecular sensitivity of PET in order to acquire quantitative data simultaneously. PET measures the distribution of radioactive substances in the human body over a scan time of several minutes. A positron-emitting radionuclide bound to a biologically active molecule (tracer) is injected into the body. The radionuclide decays in metabolic active regions and the emitted pairs of gamma rays are detected. In oncology this allows e.g. for the detection of tumor lesions. By quantification of tracer uptake, the metabolic activity of the tracer can be characterized. However, any motion between successively detected gamma rays leads to a misplacement of the detected PET event inside the body. Thus, PET quantification is impaired and lesions in the resulting PET image are blurred and

sometimes no longer visible [1]. In the past, motion correction of PET data was realized using CT [2] or PET data itself [3]. The emerge of simultaneous PET/MR system offer new possibilities to correct the motion-distorted PET data again by an MR-derived motion model which is applied to deform the PET images [4, 5, 6].

Despite various advantages of MR imaging, the low acquisition speed is one of the limiting factors for capturing three-dimensional deformations over time from a large field of view (FOV). Motion-artifact free MR acquisitions are mainly constrained by small FOVs, low image resolutions and/or patient's breathhold ability. For an accurate motion correction (MC) of PET data, a high-resolution 4D (3D + time) deformation field on a Cartesian grid is desired. Furthermore, a dynamic acquisition allowing the patient to breath freely and a retrospective flexibility to map the data to their coinciding motion state allowing a better motion adjustment, should be favored. But this on the other hand raises the need for a surrogate signal which determines the current motion state.

Several approaches exist which construct 4D images from a stack of repeated high-resolution 2D dynamic measurements [7], high-resolution 3D measurements at multiple breathhold positions [8], low-resolution 3D dynamic acquisitions [9], slice stacked 2D dynamic measurements with radial readouts [10] or dynamic 3D hybrid acquisitions with Cartesian-readout and radial-phase sampling [11]. But all of the before mentioned methods cannot meet the requirements for a dynamic 4D acquisition on a Cartesian grid.

Slice-selective MR navigator scans are often used to determine the current motion state [8, 12], but they destroy the imaged steady-state of the transversal magnetization. Therefore, self-navigation strategies [13] which extract the motion information from the acquired data deliver better imaging results.

For a dynamic (free-breathing) and Cartesian 4D acquisition, a complete coverage of the 4D sampling space for a feasible scan time is not possible. We therefore propose an acquisition scheme which subsamples the phase-encoding directions and allows the extraction of an MR navigator signal [14] (self-navigation approach). For a Compressed Sensing (CS) subsampling, the high frequency components are often sampled very sparse leading to a reduction of edge delineation

which could be very crucial for an accurate MC. Therefore, we emphasize the use of a so called Compressed Sensing Partial Subsampling (ESPRESSo) mask [15] which compacts the allowed sampling region to a smaller subset resulting in a denser sampling of the high frequency components. This acquisition scheme raises the need for a CS reconstruction. In order to improve the reconstruction quality, the motion information is incorporated into the CS reconstruction by exploiting the spatial-temporal coherence. An improved reconstructed image on the other hand also yields a more precise motion model. Hence, a joint CS and MC optimization may provide better results. Additional reference images for the motion estimation, as proposed by Jung et al. [16], are not required. Compared to Usman et al. [17] or Cao et al. [18] which combine an optical flow method with an ℓ_1 -norm minimization, our motion model is build up by a non-rigid registration and a multidimensional B-spline transformation incorporated into a reweighted ℓ_2 -norm minimization.

2. ACQUISITION

Data of the Cartesian sampling space (k-space) is continuously collected while the subject is freely breathing. In each repetition time (TR), a random sample along the two phase-encoding gradients k_y/k_z is chosen, encoded and measured. One sample can be measured multiple times, dependent on total scan time, allowing an adjustable sample to motion state assignment during the reconstruction. The sampling distribution in the k-space follows a truncated Gaussian time-invariant probability density function (pdf)

$$p(k_y, k_z) \simeq \frac{w^2}{2\pi} \exp\left(-\frac{w^2}{2} \left(\left(\frac{k_y}{M_y}\right)^2 + \left(\frac{k_z}{M_z}\right)^2\right)\right) \cdot [u(\gamma M_y - k_y) + u\left(r^2 - \left(\frac{k_y}{M_y}\right)^2 - \left(\frac{k_z}{M_z}\right)^2\right)] \quad (1)$$

where M_y and M_z are the number of phase-encoding steps along y and z . The parameter w controls the variable sampling density. The heaviside functions $u(\cdot)$ in Eq. (1) truncate the Gaussian pdf and apply a two-dimensional ESPReSSo mask [15]. With ESPReSSo, the sampling region is compacted along one phase-encoding direction to a smaller subset γM_y while a fully sampled k-space center region r ensures the Hermitean symmetry extraction in the reconstruction.

Every T_{Nav} , the MR sequence is constrained to acquire a series of $M_{y,\text{Nav}} \times M_{z,\text{Nav}}$ samples in the k-space center $k_y \in [-\frac{M_{y,\text{Nav}}}{2}, \frac{M_{y,\text{Nav}}}{2}]$, $k_z \in [-\frac{M_{z,\text{Nav}}}{2}, \frac{M_{z,\text{Nav}}}{2}]$ which can be extracted during the reconstruction and serve as a navigator signal. This navigator signal captures the current respiratory motion state as a projection of the moving liver dome over time and is used to bin the acquired samples in the gating step to their corresponding motion state. An exemplary continuously acquired sampling pattern Φ_c can be seen in Fig. 1.

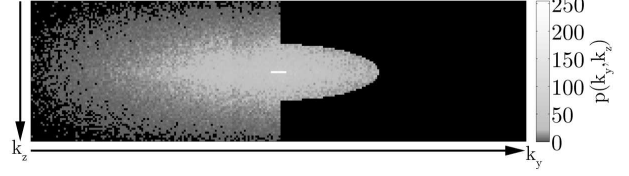


Fig. 1: Continuously acquired ESPReSSo sampling pattern Φ_c for a period of 191 s, $T_{\text{Nav}} = 200$ ms and $M_{y,\text{Nav}} = 8$, $M_{z,\text{Nav}} = 1$. Navigator samples are indicated by the solid line in the center.

3. RECONSTRUCTION

Since the subject is allowed to breath freely and the samples are acquired randomly over time, each sample must be mapped to their corresponding motion state dependent on the navigator signal. This leads to a sub-Nyquist sampled 4D k-space which raises the need for a CS reconstruction. The inter-state temporal correlation can be incorporated into a motion-compensated CS reconstruction to improve its performance whilst on the other hand this also enhances the accuracy of the multi-resolution non-rigid MC. This motivates to reformulate the reconstruction as a coupled motion-compensated CS reconstruction and motion model optimization by iteratively projecting the motion model τ onto the CS reconstruction resp. the reconstructed image ρ onto the image registration:

$$\begin{cases} \rho = \arg \min_{\rho} C_{\text{CS}}(\rho) & \text{CS reconstruction} \\ \tau = \arg \min_{\tau} C_{\text{MC}}(\tau) & \text{motion model update} \end{cases} \quad (2)$$

A low-resolution image serves as initialization for the coupled system.

3.1. Gating

Gating is a process of gathering the acquired MR samples into their corresponding motion state, based on the extracted navigator signal $s(t)$ and according to their distance to the gate centroid δ_i , $i = 1, \dots, N_G$ of the i -th motion gate g_i

$$\forall \{k_y, k_z\}: \hat{g}_i = \arg \max_i \left(\delta_i + b_i (\delta_{i+1} - \delta_i) - s(t)|_{k_y, k_z} \right) \cdot u\left(s(t)|_{k_y, k_z} - \delta_i + b_i (\delta_i - \delta_{i-1})\right) \quad i = 1, \dots, N_G \quad (3)$$

The end-expiratory gate centroid δ_1 and the end-inspiratory gate centroid δ_{N_G} are placed at the 95-th resp. 5-th percentile of all acquired samples with $P(s(t) \leq \delta_1) = 0.95$ resp. $P(s(t) \leq \delta_{N_G}) = 0.05$. The remaining $N_G - 2$ gate centroids are placed according to Lloyd's algorithm at the sample cluster centroids. A view sharing blending factor for each gate $b_i \in [\frac{1}{2}, 1]$ is introduced to flexibly tune the gate

width, ranging from no overlap ($b_i = \frac{1}{2}$) to completely overlapping gates ($b_i = 1$), and thereby adjusting the amount of shared samples between two adjacent gates to improve the SNR at the cost of an increased motion blur.

All acquired N_S 3D MR samples within one gate are collected and form together with the N_G gates the 5D tensor k-space. The large field-of-view (FOV) enabling the capture of the complete deformation within the body results in multiple N_c MR receiver coils, each covering a different part of this FOV. Thus a multi-coil 6D k-space $\boldsymbol{\nu} \in \mathbb{C}^{N_y \times N_x \times N_z \times N_G \times N_S \times N_c}$ is obtained from which the image needs to be reconstructed. Moreover, the binary sampling pattern for each motion state Φ can be obtained by binning and mapping the continuously acquired pattern Φ_c . The PET data is also gated according to the navigator signal $s(t)$ and the gate boundaries $[\delta_i - b_i(\delta_i - \delta_{i-1}), \delta_i + b_i(\delta_{i+1} - \delta_i)]$.

3.2. CS reconstruction

The linear CS reconstruction problem can be expressed in matrix form as

$$\underline{\boldsymbol{\nu}} = \mathbf{A}\underline{\boldsymbol{q}} = \Phi \mathfrak{F} \Psi \underline{\boldsymbol{q}} \quad (4)$$

where $\underline{\boldsymbol{\nu}} = \text{vec}(\boldsymbol{\nu}) \in \mathbb{C}^N$ denotes the stacked subsampled multi-coil k-space, $\underline{\boldsymbol{\rho}} \in \mathbb{C}^M$, $M = M_y M_x M_z N_G N_S N_c$ being the unknown image with its K -sparse representation $\underline{\boldsymbol{q}}$ under transformation sparsity Ψ . The Karhunen-Loève transformation acts as sparsifying transformation by compacting the sample energy within one gate and between the different motion states onto the most relevant ones. $\Phi \mathfrak{F}$ are the ESPReSSo subsampled Fourier coefficients which yields the overall system matrix $\mathbf{A} = \Phi \mathfrak{F} \Psi \in \mathbb{C}^{N \times M}$ with $N < M$. In the noise-free case, a sparse solution to the underdetermined linear system Eq. (4) can be found as

$$\min_{\underline{\boldsymbol{q}}} \|\underline{\boldsymbol{q}}\|_1 \text{ s.t. } \underline{\boldsymbol{\nu}} = \mathbf{A}\underline{\boldsymbol{q}} \quad (5)$$

where $\|\cdot\|_1$ is the ℓ_1 -norm. Due to the non-smooth nature of the ℓ_1 -norm, in contrast to other approaches [19], we recover $\underline{\boldsymbol{\rho}}$ by minimizing the ℓ_{2p} -quasi-norm with $0 < p \leq 1$ using the FOcal Underdetermined System Solver (FOCUSS) algorithm [20]. It uses an iterative affine scaling transformation (AST) realized through the weighting matrix \mathbf{W} at iteration k

$$\mathbf{W}_k = \text{diag} \left(|\underline{\boldsymbol{\rho}}_{k-1}|^p \right) \quad (6)$$

For $p = 0.5$, FOCUSS asymptotically minimizes the ℓ_1 -norm and hence converges to a sparse solution near the initialization [20]. Therefore, a low-resolution image provides a sufficient initialization. The optimization task in Eq. (5) can be formulated as a reweighted ℓ_2 -norm minimization which tries to find the optimal sparse image $\underline{\boldsymbol{q}}$ with $\underline{\boldsymbol{\rho}} = \Psi \mathbf{W} \underline{\boldsymbol{q}}$ under a data consistency constraint. In the presence of noise, the data consistency term in Eq. (4) must be relaxed towards $\|\underline{\boldsymbol{\nu}} - \mathbf{A}\underline{\boldsymbol{q}}\|_2 < \epsilon$ where ϵ denotes the standard deviation of the

input noise [21]. Furthermore, the ESPReSSo sampling strategy and the motion model update have to be accounted for as an additional constraint to the linear inverse problem.

For ESPReSSo, the k-space Hermitian symmetry $\underline{\boldsymbol{\nu}}(\underline{\boldsymbol{k}}) = \underline{\boldsymbol{\nu}}^*(-\underline{\boldsymbol{k}})$ is exploited and incorporated into the FOCUSS via a projection-onto-convex-sets (POCS) operation:

$$\begin{aligned} \Omega_1 : \underline{\boldsymbol{\nu}} &= \arg(\underline{\boldsymbol{\rho}}) \\ \Omega_2 : \underline{\boldsymbol{\rho}} &= \mathfrak{F}^{-1} \left(\mathfrak{F} (|\underline{\boldsymbol{\rho}}| \circ \exp(i\underline{\boldsymbol{\varphi}})) (\mathbf{I} - \Phi) + \Phi \underline{\boldsymbol{\nu}} \right) \end{aligned} \quad (7)$$

where $a \circ b$ denotes the Hadamard product. The solution to Eq. (7) can be considered as finding the intersection point $\Omega_1 \cap \Omega_2$ between the two convex sets Ω_1 and Ω_2 in Hilbert space H of all possible complex images. A phase estimate of the symmetrically sampled MR points $\underline{\boldsymbol{\varphi}}$ forms the first set Ω_1 which is propagated towards a data consistency term Ω_2 . The sets constrain the resulting image to lie in a closed convex subset of H . Reformulating the projection operation (7) allows framing a convex constraint for the CS minimization algorithm [22]:

$$(\Phi \underline{\boldsymbol{\nu}} + (\mathbf{I} - \Phi) \underline{\boldsymbol{\nu}}^*) = 0.5 \cdot \mathfrak{F} \left(\underline{\boldsymbol{\rho}}^* \circ e^{2i\underline{\boldsymbol{\varphi}}} + \underline{\boldsymbol{\rho}} \right) \quad (8)$$

The motion information will be considered by minimizing the residue ϵ_{res} between the end-expiratory state $\underline{\boldsymbol{\rho}}_1$ and the remaining $\underline{\boldsymbol{\rho}}_i$, $i = 2, \dots, N_G$ states. For a perfect spatial-temporal matching, i.e. optimal motion models τ_i , the residue

$$\epsilon_{\text{res}} = \sum_{i=2}^{N_G} \underline{\boldsymbol{\rho}}_1 - \tau_i \left(\underline{\boldsymbol{\rho}}_i \right) \quad (9)$$

should be small. Additionally, one can utilize the multi-coil information realized through the kernel \mathbf{G} representing linear inter-channel weights to improve the reconstruction quality, as proposed by Lustig et al. [23].

The overall cost function of the constrained optimization problem can be constructed by means of Lagrangian multiplier as a regularized FOCUSS

$$\begin{aligned} C_{\text{CS}}(\underline{\boldsymbol{q}}; \tau) &= \|\underline{\boldsymbol{\nu}} - \Phi \mathfrak{F} \Psi \mathbf{W} \underline{\boldsymbol{q}}\|_2^2 + \lambda_1 \|\underline{\boldsymbol{q}}\|_2^2 \\ &+ \lambda_2 \|\mathfrak{F} \Psi (\mathbf{W}^* \underline{\boldsymbol{q}}^* \circ e^{2i\underline{\boldsymbol{\varphi}}} + \mathbf{W} \underline{\boldsymbol{q}}) \\ &\quad - (\Phi \underline{\boldsymbol{\nu}} + (\mathbf{I} - \Phi) \underline{\boldsymbol{\nu}}^*)\|_2^2 \\ &+ \lambda_3 \left\| \sum_{i=2}^{N_G} \Psi \mathbf{W} \underline{\boldsymbol{q}}_i - \tau_i \left(\Psi \mathbf{W} \underline{\boldsymbol{q}}_i \right) \right\|_2^2 \\ &+ \lambda_4 \|(\Psi \mathbf{G} - \mathbf{I}) \mathbf{W} \underline{\boldsymbol{q}}\|_2^2 \end{aligned} \quad (10)$$

with empirically determined values $\lambda_1, \lambda_2, \lambda_3, \lambda_4 > 0$. Since $C_{\text{CS}}(\underline{\boldsymbol{q}}) \in C^1$ is continuously differentiable, an optimal solution can be reached by a linear conjugate gradient method. Using the Wirtinger derivative $\underline{\nabla} C_{\text{CS}}(\underline{\boldsymbol{q}}) = \underline{\nabla}_{\underline{\boldsymbol{q}}^*} C_{\text{CS}}(\underline{\boldsymbol{q}}, \underline{\boldsymbol{q}}^*)$ allows the calculation of the complex-valued gradient vector.

The extraction of the most significant sample for each motion state and a root sum of squares channel combination yields the reconstructed 4D image $\boldsymbol{\rho} \in \mathbb{R}^{M_y \times M_x \times M_z \times N_G}$.

3.3. Motion model update

If one inspects a normal breathing cycle, the lowest motion burden, i.e. the longest motion-stable time interval can be identified as the end-expiratory state with the corresponding image ρ_1 . All remaining states shall be registered and transformed by $N_G - 1$ parametric and non-rigid transformations τ_i to the end-expiratory state in order to find the optimal displacement field $\vartheta_i(\underline{p}) = \tau_i(\underline{p}) - \underline{p}$ for each spatial voxel $\underline{p} = [x, y, z]^T$. The MR-derived displacement field is used for the subsequent motion correction of the gated PET data. An updated motion model $\hat{\tau}_i$ of motion state i can be derived together with the reconstructed image $\rho_i \in \mathbb{R}^{M_x \times M_y \times M_z}$, $i = 2, \dots, N_G$ by minimizing the cost function

$$\hat{\tau}_i = \arg \min_{\tau_i} C_{MC}(\tau_i, \rho_1, \rho_i) = \arg \min_{\tau} -S_M(\tau_i, \rho_1, \rho_i) \quad (11)$$

under an image similarity metric S_M , defined as the Normalized Mutual Information with entropy definition according to Mattes et al. [24]. It uses B-spline Parzen windows to calculate the joint probabilities of ρ_1 and ρ_i .

The motion model τ_i uses a parametrized cubic B-spline approach as proposed in [25]

$$\tau(\underline{p}) = \underline{p} + \sum_{\underline{p}_k \in \Upsilon} \underline{\omega}_k \beta_3\left(\frac{\underline{p} - \underline{p}_k}{\sigma}\right) \quad (12)$$

\underline{p}_k are the control points of the control point set Υ with spacing σ , $\underline{\omega}_k$ are the B-spline coefficient vectors over which Eq. (11) optimizes and $\beta_3(\underline{p})$ are the cubic multidimensional B-spline polynomials.

Eq. (11) can be solved by a Quasi-Newton Broyden-Fletcher-Goldfarb-Shanno algorithm. A multi-resolution pyramid approach based on a downsampling and Gaussian filtering as proposed by Lester and Arridge [26] is used to reduce the data and transformation complexity.

4. MATERIALS AND METHODS

Coronal *in-vivo* patient data was acquired on a 3T PET/MR scanner (Biograph mMR, Siemens) using a 3D spoiled gradient echo sequence with TE = 1.23 ms, TR = 2.60 ms, Head-Feet frequency encoding direction, Left-Right phase-encoding direction, FOV = $500 \times 500 \times 360$ mm³ and a matrix size of $256 \times 256 \times 72$. Data was acquired for a total scan time of 300 s with $T_{Nav} = 200$ ms.

The images were reconstructed offline in Matlab[®] and the registration was performed using elastix [27].

The feasibility of the proposed method is shown for a motion corrected PET/MR image of a patient with liver metastases. The corrected PET image is evaluated against the non-corrected and the end-expiratory gated PET image (serving as a ground truth for a motion-free PET) in terms of PET activity concentration (PAC) and Full width at half maximum (FWHM) of a moving liver lesion.

5. RESULTS AND CONCLUSION

The reconstructed MR image ρ of the end-expiratory state with the corresponding deformation field $\vartheta_4(\underline{p})$ mapping from the end-inspiratory state to the end-expiratory state can be seen in Fig. 2 (image is not distortion corrected). A line profile through a moving lesion of the coronal PET image in Fig. 3 visualizes the motion burden and its quality enhancement by means of motion correction with values for the non-corrected/gated/corrected PET of the FWHM = 7.6/5.5/5.4 px and the PAC = 17760/12020/23920 Bq/ml. In Fig. 4 the line profiles clearly indicate the improvement regarding delineation (FWHM) and quantification (PAC). The motion-corrected PET image has a similar FWHM as the gated PET indicating the functioning of the motion correction, but a higher PAC, since all counts from different gates are combined into the motion-corrected PET. Compared to the non-corrected PET image, both FWHM and PAC are improved by 29% and 26%, respectively.

The proposed motion correction framework is able to detect motion fast and accurately, to build up a MR-derived motion model during CS reconstruction and to correct the PET images which can result in an enhanced diagnostic accuracy and confidence.

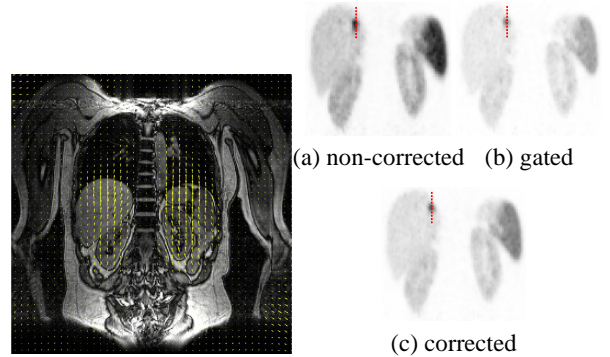


Fig. 2: MR image ρ with **Fig. 3:** PET images showing a overlaid deformation field liver lesion (bright spot) with $\vartheta_4(\underline{p})$. line profiles indicated by the dashed lines.

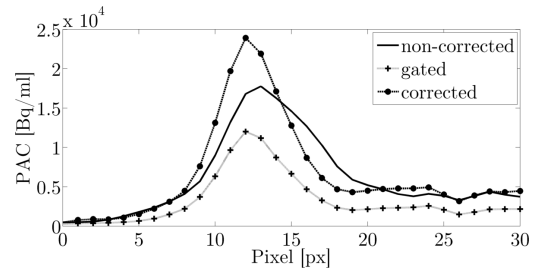


Fig. 4: Line profiles through a moving liver lesion of the non-corrected, gated and corrected PET images.

6. REFERENCES

- [1] S.A. Nehmeh and Y.E. Erdi, "Respiratory motion in positron emission tomography/computed tomography: a review," *Semin. Nucl. Med.*, vol. 38, no. 3, pp. 167–76, 2008.
- [2] H. Fayad, T. Pan, C. Roux D., and Visvikis, "A generic respiratory motion model for motion correction in pet/ct," in *Nuclear Science Symposium Conference Record (NSS/MIC), 2010 IEEE*, Oct 2010, pp. 2455–58.
- [3] S. Ambwani, W.C. Karl, A. Tawakol, and H. Pien, "Joint cardiac and respiratory motion correction and super-resolution reconstruction in coronary PET/CT," in *Biomedical Imaging: From Nano to Macro, 2011 IEEE International Symposium on*, March 2011, pp. 1702–05.
- [4] A. P. King, C. Buerger, C. Tsoumpas, P. K. Marsden, and T. Schaeffter, "Thoracic respiratory motion estimation from MRI using a statistical model and a 2-D image navigator," *Med. Image Anal.*, vol. 16, no. 1, pp. 252–64, 2012.
- [5] C. Würslin, H. Schmidt, P. Martirosian, C. Brendle, A. Boss, N.F. Schwenzer, and L. Stegger, "Respiratory motion correction in oncologic PET using T1-weighted MR imaging on a simultaneous whole-body PET/MR system," *J. Nucl. Med.*, vol. 54, no. 3, pp. 464–71, 2013.
- [6] R. Grimm, S. Fürst, M. Souvatzoglou C. Forman, J. Hutter, I. Dregely, S.I. Ziegler, B. Kiefer, J. Hornegger an KT. Block, and SG. Nekolla, "Self-gated MRI motion modeling for respiratory motion compensation in integrated PET/MRI," *Med. Image Anal.*, vol. 19, no. 1, pp. 110–20, 2015.
- [7] T. Rohlfing, C.R. Maurer, W.G. O'Dell, and J. Zhong, "Modeling liver motion and deformation during the respiratory cycle using intensity-based nonrigid registration of gated MR images," *Med. Phys.*, vol. 31, no. 3, pp. 427–432, 2004.
- [8] Y. Wang, P.J. Rossman, R.C. Grimm, S.J. Riederer, and R.L. Ehman, "Navigator-echo-based real-time respiratory gating and triggering for reduction of respiration effects in three-dimensional coronary MR angiography," *Radiology*, vol. 198, no. 1, pp. 55–60, 1996.
- [9] J.J. van Vaals, M.E. Brummer, W.T. Dixon, H.H. Tuijthof, H. Engels, R.C. Nelson, B.M. Gerety, J.L. Chezmar, and J.A. den Boer, "'Keyhole' method for accelerating imaging of contrast agent uptake," *J. Nucl. Med.*, vol. 3, no. 4, pp. 671–5, 1993.
- [10] L. Feng, R. Grimm, K.T. Block, H. Chandarana, S. Kim, J. Xu, L. Axel, D.K. Sodickson, and R. Otazo, "Golden-Angle Radial Sparse Parallel MRI: Combination of Compressed Sensing, Parallel Imaging, and Golden-Angle Radial Sampling for Fast and Flexible Dynamic Volumetric MRI," *Magn. Reson. Med.*, 2013.
- [11] C. Prieto, S. Uribe, R. Razavi, D. Atkinson, and T. Schaeffter, "3D undersampled golden-radial phase encoding for DCE-MRA using inherently regularized iterative SENSE," *Magn. Reson. Med.*, vol. 64, no. 2, pp. 514–26, 2010.
- [12] R.L. Ehman and J.P. Felmlee, "Adaptive technique for high-definition MR imaging of moving structures," *Radiology*, vol. 173, no. 1, pp. 255–63, 1989.
- [13] J.G. Pipe, "An optimized center-out k-space trajectory for multishot MRI: comparison with spiral and projection reconstruction," *Magn. Reson. Med.*, vol. 42, no. 4, pp. 714–20, 1999.
- [14] T. Küstner, C. Würslin, N.F. Schwenzer, B. Yang, and H. Schmidt, "Self-Navigated 4D Respiratory Motion Imaging Using ESPReSSo Sampling and Reconstruction," in *Proc. Intl. Soc. Mag. Reson. Med. ISMRM Workshop on Motion Correction in MRI*, 2014.
- [15] T. Küstner, S. Gatidis, C. Würslin, N.F. Schwenzer, B. Yang, and H. Schmidt, "ESPreSSo: A Compressed Sensing partial k-space acquisition and reconstruction," in *Proc. Intl. Soc. Mag. Reson. Med. ISMRM*, 2014, vol. 22, p. 1547.
- [16] H. Jung and J.C. Ye, "Motion Estimated and Compensated Compressed Sensing Dynamic Magnetic Resonance Imaging: What We Can Learn From Video Compression Techniques," *Int. J. Imaging Syst. and Technol.*, vol. 20, pp. 81–98, 2010.
- [17] M. Usman, D. Atkinson, F. Odille, C. Kolbitsch, G. Vaillant, T. Schaeffter, P.G. Batchelor, and C. Prieto, "Motion Corrected Compressed Sensing for Free-Breathing Dynamic Cardiac MRI," *Magn. Reson. Med.*, vol. 70, pp. 504–16, 2013.
- [18] C. Cao and Y. Sun, "Accelerated dynamic MRI via inter-frame motion estimation," in *IEEE 11th International Symposium on Biomedical Imaging (ISBI)*, April 2014, pp. 449–452.
- [19] P.L. Combettes and J. Pesquet, "A Douglas-Rachford Splitting Approach to Nonsmooth Convex Variational Signal Recovery," *IEEE J. Sel. Topics Signal Process.*, vol. 1, no. 4, pp. 564–74, Dec 2007.
- [20] I.F. Gorodnitsky and B.D. Rao, "Sparse signal reconstruction from limited data using FOCUSS: A re-weighted minimum norm algorithm," *IEEE Trans. Signal Process.*, vol. 45, pp. 600–16, 1997.
- [21] K. Kreutz-Delgado, J.F. Murray, B.D. Rao, K. Engan, T. Lee, and T.J. Sejnowski, "Dictionary Learning Algorithms for Sparse Representation," *Neural Comput.*, vol. 15, no. 2, pp. 349–96, 2003.
- [22] G. McGibney, M.R. Smith, S.T. Nichols, and A. Crawley, "Quantitative Evaluation of Several Partial Fourier Reconstruction Algorithms Used in MRI," *Magn. Reson. Med.*, vol. 30, pp. 51–59, 1993.
- [23] M. Lustig and J.M. Pauly, "SPIRiT: Iterative Self-consistent Parallel Imaging Reconstruction From Arbitrary k-Space," *Magn. Reson. Med.*, vol. 64, pp. 457–471, 2010.
- [24] D. Mattes, D.R. Haynor, H. Vesselle, T.K. Lewellen, and W. Eubank, "PET-CT image registration in the chest using free-form deformations," *IEEE Trans. Med. Imag.*, vol. 22, no. 1, pp. 120–28, 2003.
- [25] D. Rueckert, L.I. Sonoda, C. Hayes, D.L.G. Hill, M.O. Leach, and D.J. Hawkes, "Nonrigid Registration Using Free-Form Deformations: Application to Breast MR Images," *IEEE Trans. Med. Imag.*, vol. 18, no. 8, pp. 712–21, 1999.
- [26] H. Lester and S.R. Arridge, "A survey of hierarchical non-linear medical image registration," *Pattern Recogn.*, vol. 32, no. 1, pp. 129–49, 1999.
- [27] S. Klein, M. Staring, K. Murphy, M.A. Viergever, and J.P.W. Pluim, "elastix: A Toolbox for Intensity-Based Medical Image Registration," *IEEE Trans. Med. Imag.*, vol. 29, no. 1, pp. 196–205, Jan 2010.